The Accretion Flow Geometry of MAXI J1820+070 through Broadband Noise Research with Insight Hard X-ray Modulation Telescope

Yang, Zi Xu; Zhang, Liang; Bu, Qing Cui; Huang, Yue; Liu, He Xin; Yu, Wei; Wang, P. J.; Tao, L.; Qu, J. L.; Zhang, S. N.

Citation for published version (APA):
Yang, Z. X., Zhang, L., Bu, Q. C., Huang, Y., Liu, H. X., Yu, W., Wang, P. J., Tao, L., Qu, J. L., Zhang, S. N., Zhang, S. N., Ma, X., Song, L. M., Jia, S. M., Ge, M. Y., Liu, Q. Z., Yan, J. Z., Zhou, D. K., Li, T. M., ... Xiao, Y. X. (2022). The Accretion Flow Geometry of MAXI J1820+070 through Broadband Noise Research with Insight Hard X-ray Modulation Telescope. *Astrophysical Journal*, *932*(1), [7]. https://doi.org/10.3847/1538-4357/ac63af

The Accretion Flow Geometry of MAXI J1820+070 through Broadband Noise Research with Insight Hard X-ray Modulation Telescope

Zi-Xu Yang[1,2], Liang Zhang[1], Qing-Cui Bu[3], Yue Huang[1], He-Xin Liu[1,2], Wei Yu[1,2], P. J. Wang[1,2], L. Tao[1,2], J. L. Qu[1,2], S. Zhang[1,2], S. N. Zhang[1,2], X. Ma[1,2], L. M. Song[1,2], S. M. Jia[1,2], M. Y. Ge[1,2], Q. Z. Liu[4], J. Z. Yan[4], D. K. Zhou[1,2], T. M. Li[1,2], B. Y. Wu[1,2], X. Q. Ren[1,2], R. C. Ma[1,2], Y. X. Zhang[5], Y. C. Xu[1,2], B. Y. Ma[1,2], Y. F. Du[1,2], Y. C. Fu[1,2], and Y. X. Xiao[1,2]

[1] Key Laboratory for Particle Astrophysics, Institute of High Energy Physics, Chinese Academy of Sciences, 19B Yuquan Road, Beijing 100049, People's Republic of China; yangzx@ihep.ac.cn, zhangliang@ihep.ac.cn, qujl@ihep.ac.cn
[2] University of Chinese Academy of Sciences, Chinese Academy of Sciences, Beijing 100049, People's Republic of China
[3] Institut für Astronomie und Astrophysik, Kepler Center for Astro and Particle Physics, Eberhard Karls Universität, Sand 1, D-72076 Tübingen, Germany
[4] Purple Mountain Observatory, Chinese Academy of Sciences, Nanjing 210034, People's Republic of China
[5] Kapteyn Astronomical Institute, University of Groningen, Postbus 800, 9700 AV Groningen, The Netherlands

Abstract

Here we present a detailed study of the broadband noise in the power density spectra of the black hole X-ray binary MAXI J1820+070 during the hard state of its 2018 outburst, using Hard X-ray Modulation Telescope observations. The broadband noise shows two main humps, which might separately correspond to variability from a variable disk and two Comptonization regions. We fitted the two humps with multiple Lorentzian functions and studied the energy-dependent properties of each component up to 90–150 keV and their evolution with spectral changes. The lowest-frequency component is considered as the subharmonic of the quasiperiodic oscillation component and shows a different energy dependence compared with other broadband noise components. We found that although the fractional rms of all the broadband noise components mainly decreases with the energy, their rms spectra are different in shape. Above ∼20–30 keV, the characteristic frequencies of these components increase sharply with the energy, meaning that the high-energy component is more variable on short timescales. Our results suggest that the hot inner flow in MAXI J1820+070 is likely to be inhomogeneous. We propose a geometry with a truncated accretion disk and two Comptonization regions.

1. Introduction

Black hole X-ray binaries (BHXBs) in a complete outburst usually show a counterclockwise "q-shaped" evolution pattern in the hardness–intensity diagram (HID). The different branches of HID correspond to different spectral and temporal states (see Remillard & McClintock 2006; Belloni & Motta 2016, for reviews). At the beginning of an outburst, the source is observed in a hard state (HS), where its energy spectrum is dominated by a hard power-law component with a photon index of ∼1.5–1.7. After leaving the HS, its spectrum becomes softer. A BHXB at this stage usually goes through an intermediate state (IMS) and then reaches a soft state (SS) near the outburst peak. In the IMS, both a soft component and a hard nonthermal component contribute significantly to the energy spectrum, while in the SS the spectrum is dominated by a thermal component from an accretion disk (Shakura & Sunyaev 1973) with a weak power-law tail. During the outburst decay, a source generally follows a reverse order and evolves back to quiescence.

BHXBs typically show fast X-ray variability on a wide range of timescales (Belloni & Stella 2014; Ingram & Motta 2019). The Fourier power density spectrum (PDS) serves as a powerful tool to study the fast X-ray variability. The typical power spectrum of BHXBs in the hard state usually includes a quasiperiodic oscillation (QPO) and broadband noise. According to a different quality factor Q (Q is defined as the ratio of central frequency and width), we divide them into QPO ($Q > 2$) and broadband noise ($Q < 2$) components in the low/hard state (LHS) and intermediate state (IMS; Belloni et al. 2002). According to different central frequencies and quality factors etc., QPO can be divided into A, B, and C types. In the LHS and hard IMS, type-C QPO is believed to come from Lense–Thirring precession based on the truncated disk/hot inner flow model (Schnittman et al. 2006; Ingram et al. 2009). For other broadband continuum components, which represent fast aperiodic variability, several models have been presented to explain this noise component, including the shot noise model, coronal flare model, and fluctuation propagation model (Terrell & James 1972; Nolan et al. 1981; Belloni & Hasinger 1990; Mineshige et al. 1994; Stern & Svensson 1996). Considering that the shot noise model predicts a stationary power spectrum and cannot produce a linear rms–flux relation for different timescales, it is not accepted to explain the broadband noise (Li et al. 2012). Furthermore, Uttley (2004) showed that the rms–flux relation in the accreting millisecond pulsar SAX J1808.4-3658 is coupled with the 401 Hz pulsation. This relation put a strict constrain on the origin of the rms–flux relation from magnetic caps of the neutron star, which means that the linear relation does not favor the coronal flare model for the X-ray variability. Up to now, the fluctuation propagation model is widely accepted because it naturally

explains the rms–flux relation for different timescales, which is common in X-ray binaries (Uttley & McHardy 2001; Negoro & Mineshige 2002; Gleissner et al. 2004; Uttley 2004; Uttley et al. 2005; Li et al. 2010, 2012). In the fluctuation propagation model (Lyubarskii 1997; Ingram & Done 2012; Ingram 2016; Mushtukov et al. 2019), the broadband noise components are believed to break down at the local viscous frequency $f_{\rm visc} \propto 1/R^2$ in a power spectrum with a Lorentzian shape $1/(1 + (f/f_{\rm visc}(R))^2)$ in the PDS (Rapisarda et al. 2014, 2016a, 2016b, 2017a, 2017b; Ingram 2016; Turner & Reynolds 2021). Perturbation occurs at each radius of the accretion flow, but the fluctuation from the outer region will modulate the inner region because of the inward motion of accretion flow. This is the reason why we call it the fluctuation propagation model. Rapisarda et al. (2014) applied PROP-FLUC on BHB MAXI J1543-564 for the first time fitting the single-hump power spectrum in a single energy band. After that, Rapisarda et al. (2016a) applied PROPFLUC on BHB MAXI J1659-152 using for the first time the hypothesis of fluctuations stirred up and propagating from the disk to hot flow. They fitted simultaneously the power spectra in two energy bands and cross spectra between two bands. Rapisarda et al. (2017b) further updated PROPFLUC by introducing the hypothesis of extra variability in the hot flow, damping, and different propagation speeds of the fluctuations. Rapisarda et al. (2017a) modeled the power spectra, time lags, and coherence in the hard and soft states of Cyg X-1. Mushtukov et al. (2018) considered more realistically both forward and backward propagation for the first time and found that propagating fluctuations also produce soft lags at high frequencies as the reflection process does in numerical simulations. Mahmoud & Done (2018a, 2018b) built a spectral-timing model to explain the energy dependence of power spectra and phase-lag spectra with two Comptonization zones based on the fluctuation propagation model.

Stiele & Yu (2015) showed a noise component with a characteristic frequency above 1 Hz in the hard energy band (4–8 keV) and the same component at a lower frequency in the soft band (1–2 keV) in a large BHXB sample. The dependence was interpreted as a hint that the hard upscattered photons originate in the inner region of the Comptonizing corona whereas the soft band originates from the outer region. However, due to the detector energy band limit, only the energy band below 10 keV was implemented (Stiele & Yu 2015). Apart from the energy dependence of the characteristic frequency, in the LHS the noise is also slightly stronger at lower energies. The fractional rms of noise as a function of the energy is flat or decreases by a few percent from 2 to 20 keV (Belloni et al. 2011). In previous studies, some authors (Yu & Zhang 2013; Stiele & Yu 2014) also investigated the energy dependence of power spectra but investigation was limited to a narrow energy range. It is necessary to provide more information about the high-energy dependence of broadband noise. As a result, we present a wider-range energy band dependence in more detail with the help of the Insight Hard X-ray Modulation Telescope (HXMT) low-energy, medium-energy, and high-energy detectors for the first time.

MAXI J1820+070 is a new X-ray transient discovered on 2018 March 11 by the Monitor of All-sky X-ray Image (MAXI) Gas Slit Camera (Matsuoka et al. 2009; Kawamuro et al. 2018). Optical follow-up observations identified an optical counterpart coinciding with ASASSN-18ey (Denisenko 2018). Torres et al. (2019) derived a mass function $f(M) = 5.18 \pm 0.15\,M_\odot$, dynamically confirming the black hole nature of the source. Torres et al. (2020) estimated the mass of the black hole to be $5.73 < M(M_\odot) < 8.34$ under 95% confidence level limits. A precise distance of 2.96 ± 0.33 kpc was obtained from radio parallax (Atri et al. 2020), with a jet inclination angle $i = 63^\circ \pm 3^\circ$. The similar distance result $D = 2.81^{+0.70}_{-0.39}$ kpc was obtained by Gaia Early Data Release 3 parallax measurement (Bailer-Jones et al. 2021). By fitting the temperature and radius of the donor, Mikolajewska et al. (2022) also constrained the distance at $D \approx 3$ kpc. MAXI J1820+070 is likely to harbor a slowly spinning black hole. Guan et al. (2021) constrained the spin of the black hole to be $a_* = 0.2^{+0.2}_{-0.3}$ by fitting the Insight-HXMT broadband spectra. A similar low-spin result $a_* = 0.14 \pm 0.09$ was obtained by Zhao et al. (2021).

During the outburst, MAXI J1820+070 stayed in the HS for almost 4 months from 2018 March to early 2018 July. The unchanging shape of the Fe line profile (Buisson et al. 2019), together with the shortening thermal reverberation lags, suggest that the HS evolution is driven by the changes of the corona, rather than the disk (Kara et al. 2019). However, several recent results are inconsistent with this picture and support a truncated disk geometry (De Marco et al. 2021; Dzielak et al. 2021). Type-C QPOs were detected in optical and X-ray wavelengths (Fiori et al. 2018; Yu et al. 2018; Zampieri et al. 2018; Stiele & Kong 2020; Ma et al. 2021; Thomas et al. 2022). Starting from 2018 July 4 (MJD 58303), the source underwent a rapid hard-to-soft transition. During the transition, an extremely powerful superluminal ejection was detected (Bright et al. 2020) close in time to the appearance of the type-B QPO (Homan et al. 2020). After the transition, the source moved to the SS and stayed there for over 2 months before the final soft-to-hard transition (see Stiele & Kong 2020 for the details of the outburst evolution).

Dzielak et al. (2021) studied the properties of the broadband noise in the PDS of MAXI J1820+070 with Neutron Star Interior Composition Explorer (NICER) data. They found that the broadband noise can be fitted with four Lorentzians, and the spectra of these variability components are quite different in shape. At least two Comptonization regions with different temperatures and optical depths are required to fit both the variability spectra and the time-averaged spectra. Kawamura et al. (2022) proposed a model based on the fluctuations propagation by considering that the hot inner flow is spectrally inhomogeneous, and the viscous timescale is discontinuous between the disk and the hot flow. This model reconstructs the shape of the broadband noise below 10 keV in MAXI J1820 +070. The large effective area of Insight-HXMT at high energies enables us to perform detailed analysis on fast X-ray variability at energy bands above 100 keV (e.g., Huang et al. 2018, 2021; Liu et al. 2020, 2021). In Ma et al. (2021), the authors reported the discovery of low-frequency QPOs above 200 keV in MAXI J1820+070 for the first time. In this work, we present a qualitative study of the evolution of the broadband noise and its energy dependence using Insight-HXMT observations of MAXI J1820+070. For the first time, we extend the study of the broadband noise up to 100–150 keV. In Section 2, we describe the observation and data reduction. The analysis and main results are presented in Section 3 and discussed in Section 4. In Section 5, we summarize our results.
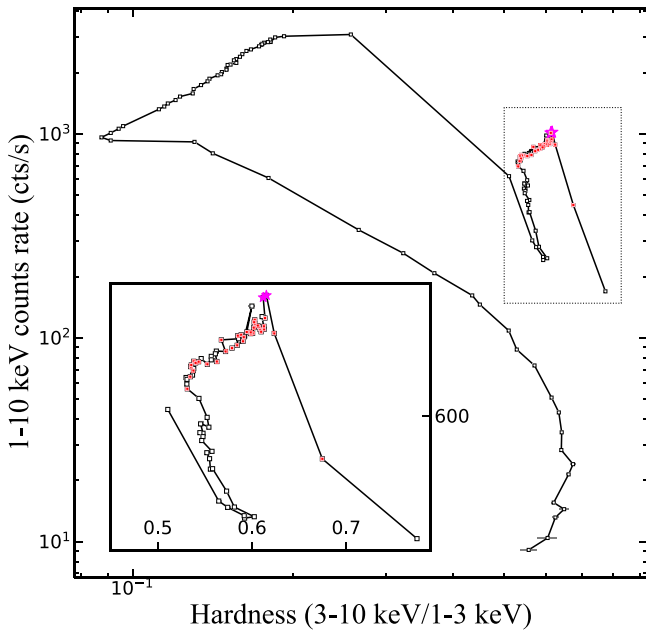
Figure 1. Insight-HXMT hardness–intensity diagram (HID). The red points mark the observations used in this work to study the evolution of the different PDS components with the hardness. The magenta points mark the observations we used to study the energy-dependent properties of these components.

2. Observations and Data Reduction

Insight-HXMT is China's first X-ray astronomy satellite, launched on 2017 June 15 (Zhang et al. 2020). It carries three slat-collimated instruments: the high-energy X-ray telescope (HE: 20–250 keV; Liu et al. 2020), the medium-energy X-ray telescope (ME: 5–30 keV; Cao et al. 2020), and the low-energy X-ray telescope (LE: 1–15 keV; Chen et al. 2020).

Four days after the discovery of MAXI J1820+070, Insight-HXMT started monitoring MAXI J1820+070 at a high cadence. During its initial full outburst between 2018 March and October, Insight-HXMT accumulated a total exposure of 2560 ks. The LE (1–10 keV), ME (10–30 keV), and HE (30–150 keV) light curves of this outburst have been shown in Ma et al. (2021). In Figure 1, we show the HID of this outburst. For our analysis, we only selected observations with LE exposure times longer than 2500 s and LE counts rate larger than 440 counts s^{-1}, where their PDS show significant broadband noise and there are enough photons to perform detailed timing analysis. Table 1 lists the log of the observations used in this work.

The data are extracted from all three instruments using the Insight-HXMT Data Analysis software (HXMTDAS) v2.04,[6] and filtered with the following criteria: (1) pointing offset angle less than 0°.04; (2) Earth elevation angle larger than 10°; (3) value of the geomagnetic cutoff rigidity larger than 8 GV; (4) at least 300 s before and after the South Atlantic Anomaly passage. To avoid possible contamination from the bright Earth and nearby sources, we only use data from the small field of view (Chen et al. 2018).

Table 1
Log of Insight-HXMT Observations Used in This Work

ObsID	Start Time (UTC)	Exposure (s)	Hardness	QPO
P0114661002	2018/03/16 10:01:24	32717	0.67(1)	None
P0114661003	2018/03/22 10:46:58	23245	0.62(1)	C
P0114661004	2018/03/24 07:19:14	28893	0.61(1)	C
P0114661005	2018/03/20 00:00:10	6343	0.62(1)	C
P0114661006	2018/03/27 08:29:37	3325	0.61(1)	C
P0114661008	2018/03/29 20:56:55	4649	0.61(1)	C
P0114661009	2018/03/30 16:02:31	3728	0.61(1)	C
P0114661010	2018/03/31 20:41:05	5356	0.61(1)	C
P0114661011	2018/04/01 20:33:24	26322	0.61(1)	C
P0114661012	2018/04/03 23:29:38	8122	0.61(1)	C
P0114661013	2018/04/05 20:04:33	8490	0.61(1)	C
P0114661014	2018/04/06 15:11:06	12809	0.60(1)	C
P0114661015	2018/04/08 13:22:00	8151	0.60(1)	C
P0114661016	2018/04/09 10:04:01	5744	0.60(1)	C
P0114661017	2018/04/10 14:43:27	8337	0.60(1)	C
P0114661018	2018/04/11 20:58:02	7313	0.60(1)	C
P0114661019	2018/04/12 16:03:53	9654	0.60(1)	C
P0114661020	2018/04/14 11:01:36	7600	0.60(1)	C
P0114661021	2018/04/15 01:20:44	2992	0.59(1)	C
P0114661024	2018/04/18 15:14:50	7265	0.59(1)	C
P0114661025	2018/04/19 15:06:26	7360	0.59(1)	C
P0114661026	2018/04/20 14:58:02	6492	0.59(1)	C
P0114661027	2018/04/23 19:19:13	2812	0.58(1)	C
P0114661028	2018/04/25 14:16:17	4639	0.58(1)	C
P0114661029	2018/04/27 09:13:33	4215	0.58(1)	C
P0114661031	2018/04/22 19:27:34	4025	0.58(1)	C
P0114661032	2018/04/28 13:51:51	4029	0.57(1)	C
P0114661035	2018/05/02 10:09:17	3617	0.56(1)	C
P0114661038	2018/05/05 09:46:03	2817	0.56(1)	C
P0114661040	2018/05/07 11:05:59	2719	0.55(1)	C
P0114661041	2018/05/08 10:58:08	5513	0.54(1)	C
P0114661042	2018/05/09 14:01:08	2632	0.54(1)	C
P0114661043	2018/05/10 13:53:07	2633	0.54(1)	C
P0114661044	2018/05/12 04:04:08	3950	0.54(1)	C
P0114661045	2018/05/13 00:45:01	2729	0.54(1)	C
P0114661048	2018/05/16 13:03:38	3388	0.54(1)	C
P0114661052	2018/05/20 15:41:03	15578	0.53(1)	C

Note. The hardness is the ratio of the count rate between the 1.0–3.0 keV and the 3.0–10.0 keV bands.

3. Analysis and Results

To study the fast X-ray variability, we produce PDS from different energy bands for each observation we used. We use 128 s long intervals and 1/256 s time resolution, corresponding to a Nyquist frequency of 128 Hz. The PDS is then applied to Miyamoto normalization, namely, it is normalized to the fractional rms (Miyamoto et al. 1991). In Figure 2, we show representative PDS for LE (1–10 keV), ME (10–30 keV), and HE (30–150 keV), respectively. The PDS of ME and HE are separately multiplied by a factor of 1.4 and 2.1 to keep the QPO aligned between energy bands. The PDS we show here are extracted from two relatively long observations (ObsIDs P0114661003 and P0114661004) with a similar PDS shape. It is apparent from this figure that, although the shape of the noise component below the QPO frequency has not changed too much, the shape of the noise component above the QPO frequency changes significantly between energies. In order to further study the properties of the QPO and the broadband noise, we fit the PDS with a multiple-Lorentzian model
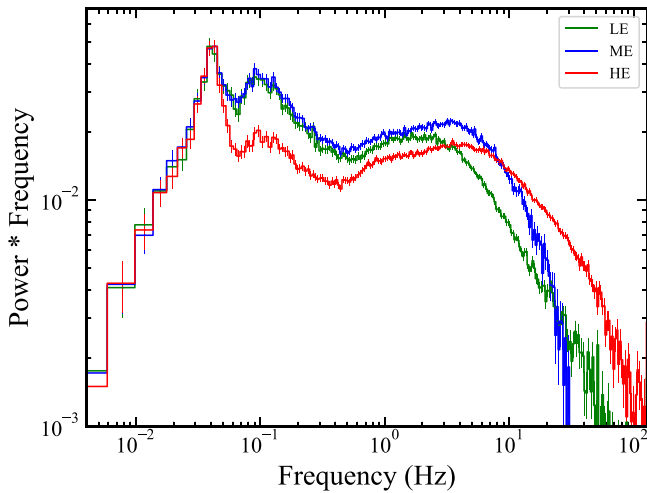

Figure 2. Representative PDS for LE (1–10 keV), ME (10–30 keV), and HE (30–150 keV), respectively. The PDS are calculated using the data of ObsIDs P0114661003 and P0114661004. The PDS of the two observations have a similar shape and consistent fractional rms of different energy bands. The PDS of ME and HE are separately multiplied by a factor of 1.4 and 2.1 to keep the QPO aligned between energy bands.
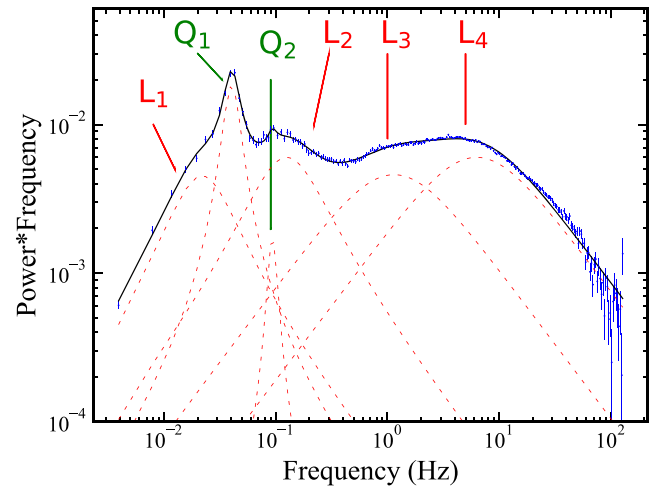

Figure 3. A representative PDS of HE (30–150 keV) plotted along with the best multi-Lorentzian fit (red). The PDS are calculated using the data of ObsIDs P0114661003 and P0114661004, and fitted with a multiple-Lorentzian model. Q_1 and Q_2 represent the QPO and its second harmonic, respectively. L_1, L_2, L_3, and L_4 represent the four broadband noise components on different timescales.

(Belloni et al. 2002). In Figure 3, we show a representative PDS of the HE (30–150 keV) band with its best fit. The QPO and its second harmonic are fitted with one Lorentzian each (Q_1 and Q_2). The broadband noise shows a two-humped shape and can be well-fitted with four Lorentzians, i.e., a very low-frequency noise (L_1), a low-frequency noise (L_2), and two high-frequency noise components (L_3 and L_4). After the fitting process, we calculate the characteristic frequency and the fractional rms amplitude for each component. The characteristic frequency, $\nu_{\max}$, is defined as $\nu_{\max} = \sqrt{\nu_0^2 + (\sigma/2)^2}$, where ν_0 is the centroid frequency, and σ is the FWHM of the Lorentzian function (Belloni et al. 1997).

In order to study the energy-dependent properties of the different components, we extract the PDS from 12 energy bands: LE (1–3, 3–7 keV), ME (7–10, 10–20, 20–30 keV), HE (30–40, 40–50, 50–60, 60–70, 70–80, 80–90, 90–150 keV). In this paper, we only show the results combined from ObsIDs P0114661003 and P0114661004. The energy-dependent properties of the other observations are similar.

3.1. Properties of L_1

Figure 4 shows the energy dependence of the fractional rms and characteristic frequency of L_1. The characteristic frequency of L_1 remains more or less constant in the 1–150 keV energy band. This is similar to what was found in Ma et al. (2021) for the QPO and its second harmonic. The evolution of the fractional rms of L_1 with the energy is more complicated. Below ∼30 keV, the fractional rms shows a slight decreasing trend with the energy, while above ∼30 keV, the fractional rms increases monotonously with the energy.

In Figure 5 we show the characteristic frequency of the QPO as a function of the characteristic frequency of L_1. It can be seen that the data points follow the correlation $\nu_{\rm QPO} = 2\nu_{L_1}$, rather than the WK correlation found by Wijnands & van der Klis (1999) and Bu et al. (2017) in other BHXRBs. In LHS, the correlation between the characteristic frequencies of QPO and low-frequency broadband noise can be fitted by a power-law function, the so-called WK correlation. This suggests that L_1 is more like a subharmonic of the QPO rather than broadband
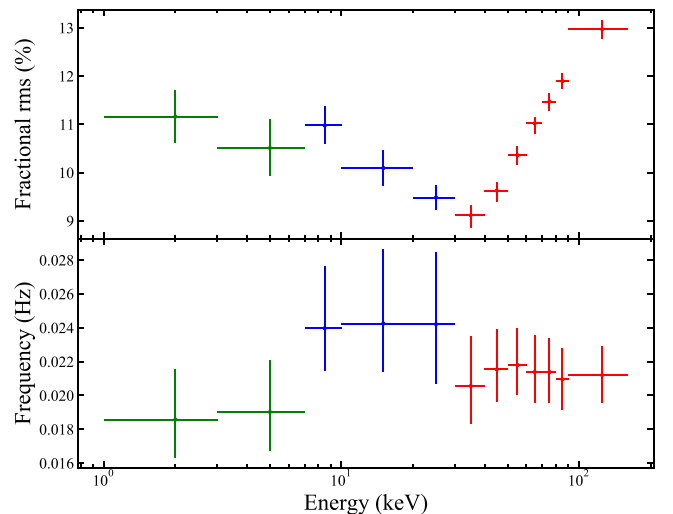

Figure 4. Energy dependence of the fractional rms and characteristic frequency of L_1. The green, blue, and red points represent the LE, ME, and HE data, respectively. The characteristic frequency does not show significant changes with the energy. Therefore, we fixed the centroid frequency and FWHM of L_1 when calculating the energy dependence of the fractional rms. The data are extracted from ObsID P0114661003 and P0114661004.

noise. We have tried to fit the low-frequency part of the PDS (below the QPO frequency) with two Lorentzian functions. However, adding another Lorentzian does not improve the fits a lot, and this extra component is not statistically needed. Note that, the quality factor for L_1 is relatively low (<1) compared with QPO Q_1 and harmonic Q_2.

In order to compare the fractional rms relation between L_1 and Q_1, we show the rms(E) of QPO and the ratio of rms between Q_1 and L_1 in Figure 6. The ratio keeps almost constant at 1.2–1.3 when the energy is lower than 30 keV. However, when the energy is higher than 30 keV, the ratio starts to decline sharply from 1.3 to 0.9.
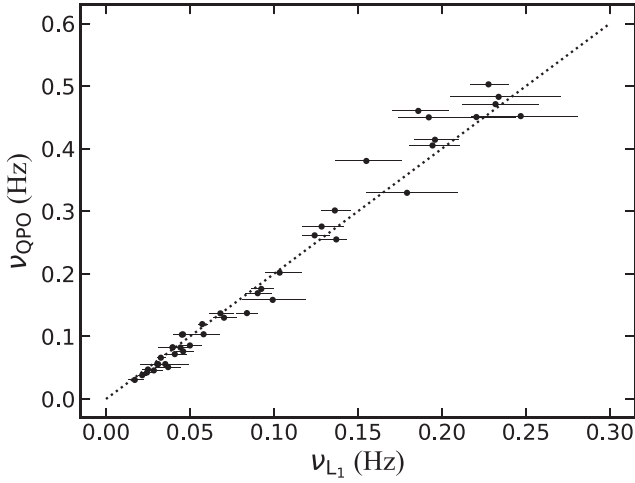
Figure 5. Characteristic frequency of the QPO as a function of the characteristic frequency of L_1. The dotted line represents the correlation $\nu_{QPO} = 2\nu_{L_1}$. The characteristic frequencies are measured by fitting the PDS of the HE band.

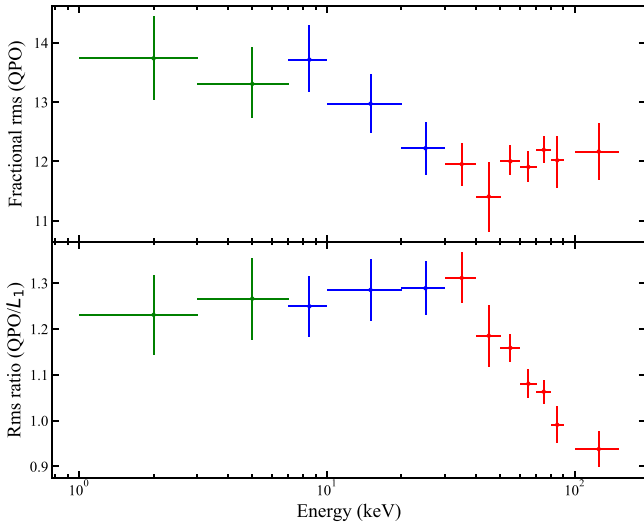**Figure 6.** Fractional rms of QPO (top panel) and ratio of fractional rms between QPO and L_1 (bottom panel) vs. energy band. The data are extracted from ObsID P0114661003 and P0114661004.

Figure 7. Evolution of the fractional rms of L_1, L_2, L_3, and L_4 with the hardness. From top to bottom, the fractional rms is calculated in the LE (1–10 keV), ME (10–30 keV), and HE (30–150 keV) bands, respectively.

3.2. Properties of L_2, L_3, and L_4

3.2.1. Evolution with Spectral Hardness

Hereafter we mainly focus on the noise components above the QPO frequency. Figure 7 shows the evolution of the fractional rms of L_2, L_3, and L_4 with the hardness ratio. From top to bottom, the rms are calculated in the LE (1–10 keV), ME (10–30 keV), and HE (30–150 keV) bands, respectively. In all panels, the hardness ratio is defined as the ratio of the count rate between the 1–3 keV and the 3–10 keV bands. In the LE and ME bands, the fractional rms of all three components generally decrease as the spectrum softens. However, in the HE band, the evolution of the fractional rms is more complicated. In the hardness range ∼0.54–0.60, the fractional rms of L_2 and L_3 increases with the hardness, while the fractional rms of L_4 remains almost constant. In the hardness range ∼0.60–0.62, the fractional rms of L_2 and L_3 instead tends to decrease, whereas the fractional rms of L_4 starts increasing sharply. In the hardness range >0.62, we do not have a good monitoring
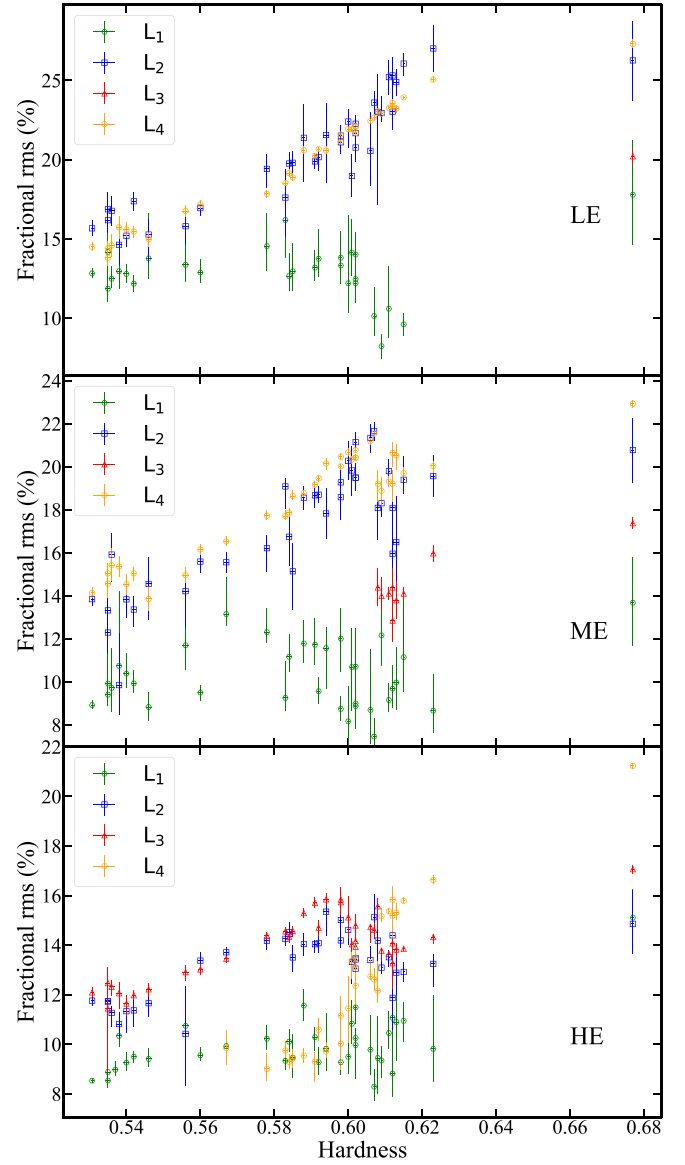
coverage. Overall, it seems that the fractional rms of all three components shows an increasing trend with the hardness.

Figure 8 shows the corresponding evolution of the characteristic frequencies of the three components with the spectral hardness. It can be seen that the characteristic frequencies of all three components generally increase as the spectra softens. At hardness >∼0.62, the increasing trend seems to be flatter than that at hardness <∼0.62.

It is worth noting that L_3 is not always present in all cases. In the PDS of LE, L_3 is only seen in the observation (ObsID P0114661002) where the spectrum is the hardest. In the PDS of ME, it only appears when the hardness ratio is larger than ∼0.61. While in the HE band, we can see this component in all observations.

Except for the evolution trend with the hardness ratio for L_2, L_3, and L_4, we also plot the evolution of the fractional rms, characteristic frequency for the L_1 component in Figures 7 and 8. As we can see from Figure 7, the fractional rms of L_1 shows no obvious evolutionary trend with the hardness ratio, which is
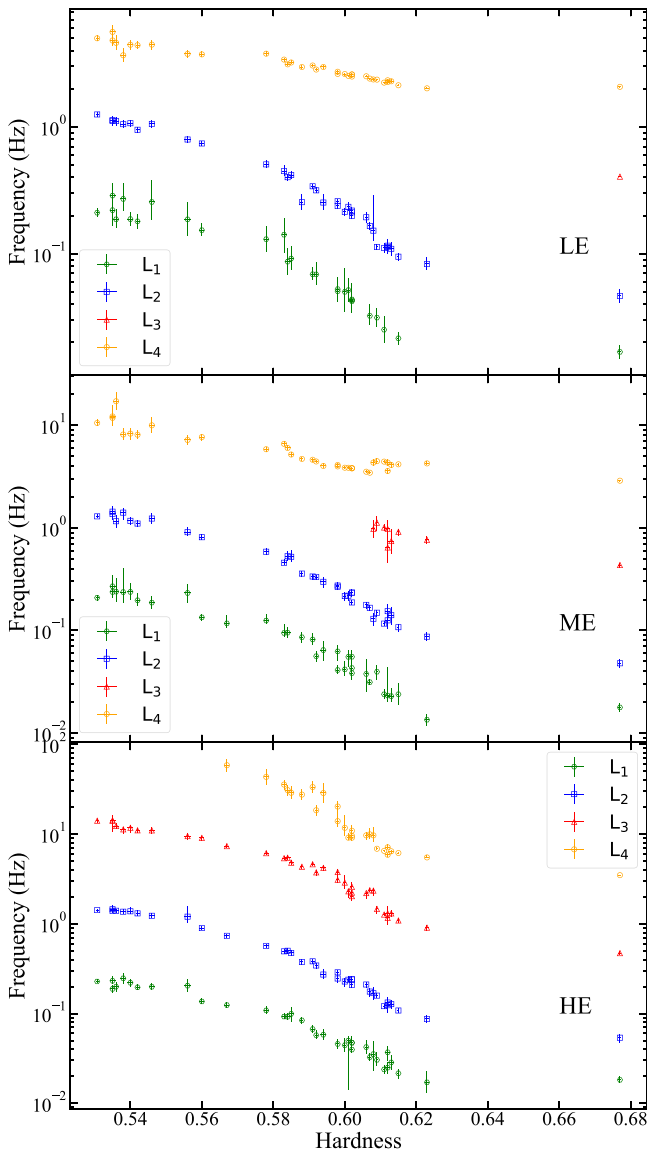
Figure 8. Evolution of the characteristic frequencies of L_1, L_2, L_3, and L_4 with the hardness.

totally different from other broadband noise components. On the contrary, from Figure 8, the evident decreasing trend of L_1 implicates the physical relation between the radiation region and spectral evolution.

3.2.2. Energy-dependent Properties

Figure 9 shows the energy dependence of the fractional rms and characteristic frequency of L_2 (left), L_3 (middle), and L_4 (right). As we can see from the right panel of Figure 9, the fractional rms decreases from 23% to 15% with increasing energy while the characteristic frequency always increases with the energy. In the left panel (L_2), the fractional rms shows the same trend, but the characteristic frequency first keeps almost constant below 20–30 keV, whereas above 20–30 keV, the frequency increases rapidly with the energy. This case is also true in the middle panel (L_3), although with a large uncertainty below 20 keV. It is worth noting that the characteristic frequency of L_4 above 90 keV is almost five times the frequency in 1–10 keV (from ~2 to ~10 Hz). Similar results

in the LE band can be found in Kawamura et al. (2022). They used NICER data to study the relationship between the asymmetric Lorentzian functions P1 and P2 and the energy that actually reflects the evolution of the characteristic frequency with the energy for the L_2, L_3, and L_4 components (P1 corresponds to L_2; P2 corresponds to L_3 and L_4).[7] In order to fit the PDS phenomenally, Kawamura et al. (2022) used two asymmetric Lorentzian functions. Nevertheless, considering the Lorentzian function that fluctuation propagation predicts, we decide to use three standard Lorentzian functions to fit the PDS.

In order to compare the relation between the fractional rms of L_2, L_3, and L_4, Figure 10 shows the energy dependence of the fractional rms ratio for three different Lorentzian components. As we can see from Figure 10, with increasing energy, when the energy is below 20–30 keV, the ratio between L_3 and L_2 changes slightly and is less than 1. When the energy is higher than 20–30 keV, the rms ratio starts to increase robustly to 1.8. As for L_4 and L_3, unlike L_2, there is a totally different trend. The rms ratio between L_4 and L_3 decreases from 1.6 to 1.1 with increasing energy. Although the downward trend is opposite to the upward trend for L_3/L_2, the rms ratio is still larger than 1, which means L_4 is more variable than L_3 at the high-energy band.

3.3. Phase-lag Spectra

Figure 11 shows a representative power spectrum and corresponding phase-lag spectrum. At higher frequencies above the QPO frequency, hard lag features are prominent. In logarithmic coordinates, the shape of the hard lag is similar to a normal distribution with large normalization plus another normal function with small normalization at low frequencies (see Figure 11). We will only focus on the high-frequency (higher than the QPO frequency) part corresponding to the broadband noise components. Then we use two log-normal functions to fit the hard lag part to get the peak value frequency of two log-normal functions (hereafter called ν_{g1} and ν_{g2}). Meanwhile, we can approximately see that $\nu_{g1} \simeq \nu_{L3}$ and $\nu_{g2} \simeq \nu_{L2}$. Then, we produce the phase-lag spectrum for different energy bands, with reference to the 1–10 keV band (Nowak et al. 1999; Altamirano & Méndez 2015; Zhang et al. 2017). The phase-lag spectra are similar between different energy bands as Figure 11 shows and have a similar shape as the phase-lag spectra given by Ma et al. (2021). As Figure 12 clearly shows, as the photon energy increases, the phase-lag peak value for two normal functions also increases with the energy band.

4. Discussion

In this paper, we have investigated the evolution of broadband noise in the PDS of MAXI J1820+070 using observations from Insight-HXMT. We uncover the possible subharmonic component, L_1, and find the different energy dependence of the fractional rms and characteristic frequency. We extend the study of the energy-dependent broadband noise up to 90–150 keV for the first time. It is found that the fractional rms of L_2, L_3, and L_4 generally increases with the hardness in the LE/ME/HE bands, whereas the characteristic frequency decreases with the hardness. As for the energy

---

[7] The ObsID we choose and that selected by Kawamura et al. (2022) are no more than one day apart, so we can easily match P1 and P2 with L_2, L_3, and L_4. P1 corresponds to L_2; P2 corresponds to L_3 and L_4.
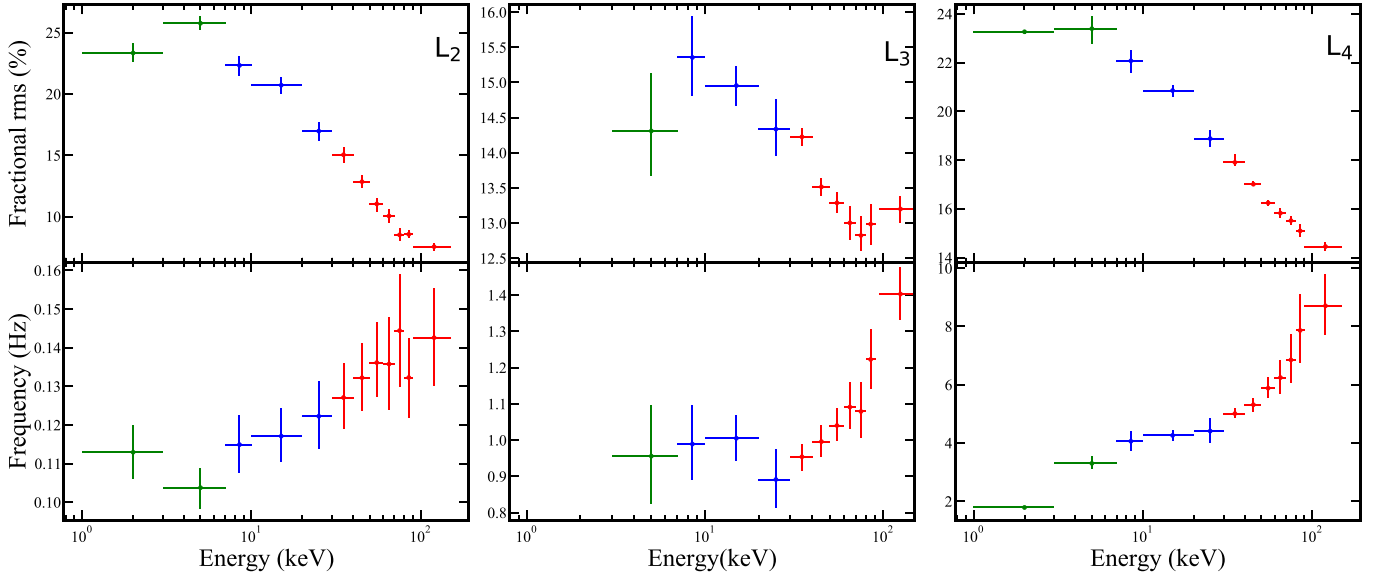
Figure 9. Energy dependence of the fractional rms and characteristic frequency for L_2 (left), L_3 (middle), and L_4 (right). Green, blue, and red points represent the LE, ME, and HE data, respectively.
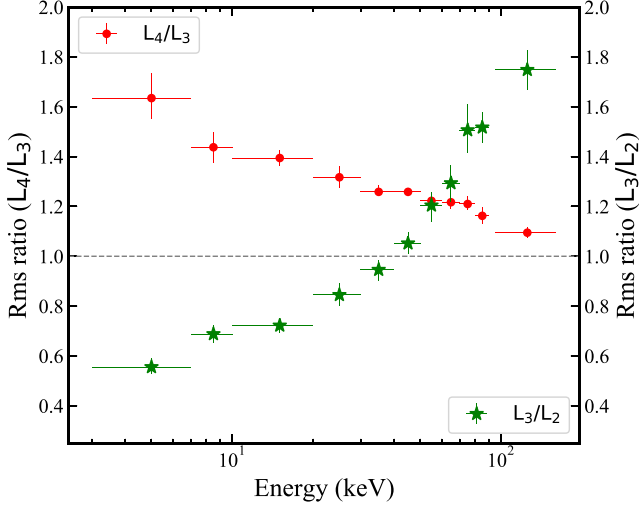

Figure 10. Ratio of fractional rms between L_2 and L_3 (green points), L_3 and L_4 (red points) vs. energy band. The data points are extracted from ObsID P0114661003 and P0114661004.
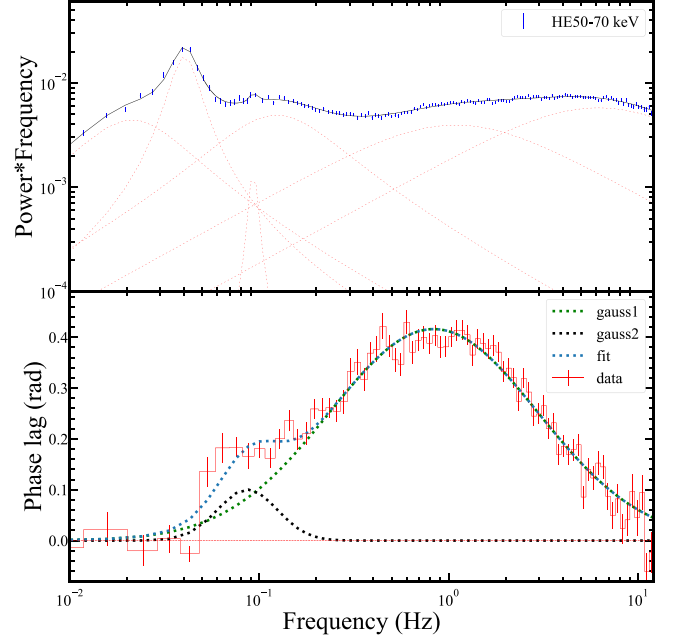

Figure 11. PDS for HE 50–70 keV and phase-lag spectrum. The phase-lag spectrum was calculated for the LE 1–10 keV relative to the HE 50–70 keV. Insight-HXMT ObsIDs P0114661003 and P0114661004 are used.

dependence, the rms of all three components decreases with energy. In particular, the characteristic frequencies of L_2 and L_3 remain unchanged below 20–30 keV and then increase to 150 keV. The characteristic frequency of L_4 always increases with the energy from 1 to 150 keV.

4.1. Properties of L_1

As shown in Section 3.1, we suggest that the peak of L_1 is observed at half the QPO frequency. This implies that the L_1 component is a subharmonic of the QPO with a low Q value. In the jet precessing model proposed by Ma et al. (2021), the QPO signal is believed to originate from the precession of a small-scale jet to explain the low-frequency QPO (LFQPO) high energy, soft lag and maximum value, and energy-related behaviors of the frequency, fractional rms, and phase lag. As a result, considering the tight relation in Figure 5, we suggest that L_1 has the same origin as a small-scale jet. However, we cannot provide a physical model to interpret the QPO and harmonics

components at the same time (Rao et al. 2010; Ratti et al. 2012). Considering the poor understanding for harmonics and that our study mainly focuses on the broadband noise component, we will mainly discuss L_2, L_3, and L_4.

4.2. Evolution of the Fractional rms and Characteristic Frequency with the Hardness

As shown in Figure 8, the characteristic frequencies of all high-frequency components (L_2, L_3, and L_4) increase with the spectral softening. This is consistent with the evolution trend commonly found in other BHXBs (Psaltis et al. 1999; Bult & van der Klis 2015; Zhang & Yu 2015). The trend of the characteristic frequency to increase with the spectral softening
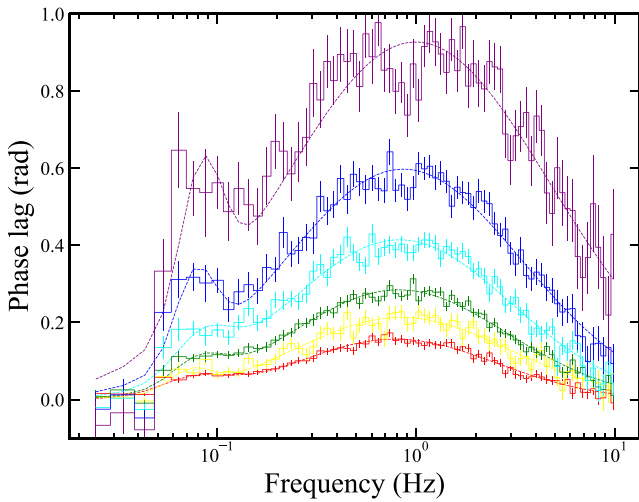
Figure 12. Phase-lag spectrum for Insight-HXMT ObsIDs P0114661003 and P0114661004. The reference energy band is 1–10 keV. From bottom to top: 10–20 keV (red), 20–30 keV (yellow), 30–50 keV (green), 50–70 keV (cyan), 70–100 keV (blue), 100–150 keV (purple) separately.

Figure 13. Truncation radius of accretion disk from the black hole as a function of the photon energy for the L_2 component. The standard $\alpha-$disk model was applied. A parameter set was used: $\alpha = 0.1$, $M = 10 M_\odot$, scale height $H/r = 0.1$.

can be explained naturally under the truncated disk/corona geometry (Esin et al. 1997; Done et al. 2007). In the truncated disk model, the outer part of the accretion flow forms a geometrically thin, optically thick accretion disk truncated at a larger radius. The inner part of the flow is a hot, geometrically thick, and optically thin configuration. The reduction in the hardness ratio generally means a higher accretion rate; thus the corona and disk should also move closer to the black hole (Belloni et al. 2005; Belloni 2010). In the fluctuation propagating model proposed by Lyubarskii (1997) and Kotov et al. (2001), the characteristic frequency is related to the outer radius of the hot flow, and as the accretion rate increases, the characteristic frequency increases while the outer radius decreases. Hence the viscous frequency of each component also increases with decreasing hardness.

In view of the fractional rms, with increasing hardness, the fractional rms also increases in L_2, L_3, and L_4. Based on the truncated disk/corona model, the corona shows more variability than a standard accretion disk (Sobolewska & Życki 2006; Axelsson et al. 2013). Consequently, when the hardness ratio increases, more corona components contribute a higher fractional rms value.

In summary, the different components show similar evolutionary trends for the fractional rms and characteristic frequency with the hardness ratio in the LE/ME/HE energy bands. The evolutionary trend can be explained under the truncated disk/corona model (Esin et al. 1997; Done et al. 2007). Actually, there is still debate on the truncation of the accretion disk in MAXI J1820+070. Buisson et al. (2019) discovered a steady inner accretion disk measured by relativistic reflection. Kara et al. (2019) found that the reverberation time lags between the continuum-emitting corona and the irradiated accretion disk are much shorter than previously seen in truncated accretion disks, and the timescale of the reverberation lags is shortened by an order of magnitude over a period of weeks, whereas the shape of the Fe Kα emission line remains remarkably constant. Similar results are also obtained from spectral analysis. Meanwhile, there are some other studies that support the truncated accretion disk argument by either spectral analysis or timing analysis (De Marco et al. 2021; Marino et al. 2021; Zdziarski et al.
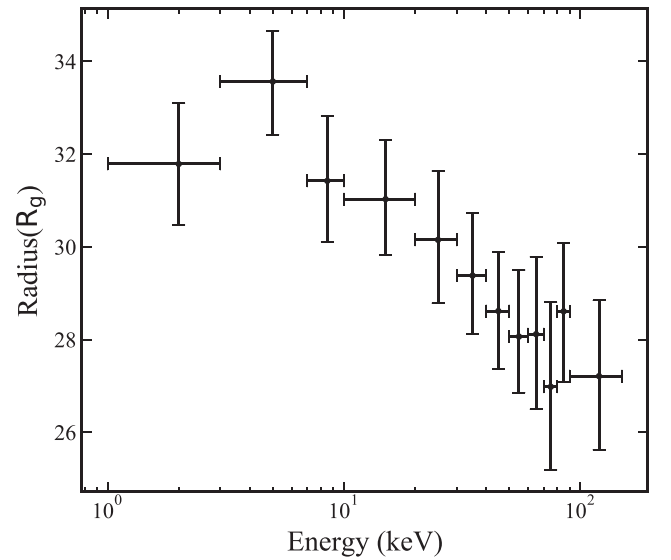
2021a, 2021b). De Marco et al. (2021) found that the frequency of the thermal reverberation lags increases steadily, and, on the other hand, the temperature of the quasi-thermal component grows as the source softens, which can be explained in terms of a decrease in the disk inner radius. Moreover, De Marco et al. (2021) measured that the values of the lag amplitude are a factor of 3 longer than those reported in Kara et al. (2019). The longer lags might not be easily reconciled with the conclusion of a disk extending close to the innermost stable circular orbit. Zdziarski et al. (2021a, 2021b) confirmed the existence of an optically thick disk of at least $>10 R_g$ from joint spectral analysis. To sum up, so far, all arguments in favor of the nontruncated disk model can be reasonably explained under the truncated disk model. Except for the methods mentioned above, in the present paper, we confirm the truncated accretion disk model in MAXI J1820+070 from the evolutionary trend of broadband noise components with a new perspective by means of the correspondence relation between break frequency and radiation region radius. Quantitatively, we can calculate the radiation region at a different energy band of L_2, which represents the variable emission from the outermost region (see Figure 13). We take a parameter set for a standard α-disk ($\alpha = 0.1$, $M_{BH} = 10 M_\odot$, scale height $H/r = 0.1$) to calculate the viscous frequency at a certain radius (Kato et al. 2008). As Figure 13 shows, the characteristic frequency of the L_2 component shows an energy dependence: the emitting region spans from $\sim 34 R_g$ to $\sim 27 R_g$ corresponding to 1–150 keV photon energy. Like Dziełak et al. (2021) and Kawamura et al. (2022) found using frequency-resolved spectral analysis that the L_2 component is supposed to come from variable disk emission. However, making use of the ME and HE data from Insight-HXMT, we actually detect high-energy emission >100 keV from the L_2 component, which cannot be attributed to a simple standard accretion disk. Considering the change of radius plotted in Figure 13, even though we can attribute the high-energy emission to the propagation of fluctuation from the disk to the hot flow, we should also expect a constant characteristic frequency for L_2 at the high-energy band according to fluctuation propagation. The characteristic

frequency of L_2 remains unchanged below 20–30 keV as Kawamura et al. (2022) found the constant peak frequency for P1. However, when the photon energy is greater than 20–30 keV, the radiation radius of L_2 starts to decrease to $27R_g$. This phenomenon cannot be easily interpreted by fluctuation from a disk propagating to the hot flow. Therefore, we speculate that L_2 may originate in a warm extended variable disk region. We therefore should consider a more complicated accretion flow geometry where a standard accretion disk transits to a hot advection-dominated accretion flow geometry.

4.3. Energy Dependence of Broadband Noise

First, the fractional rms of L_2, L_3 and L_4 all generally show decreasing trend with energy. This phenomenon also exists for another black hole transient MAXI J1348-630 for the broadband noise component in the LHS (Huang et al. 2021). This phenomenon, where the fractional rms decreases with the energy, can be interpreted as a variable-input soft-photon flux connected with the Comptonization process (Gierliński & Zdziarski 2005). Generally speaking, this can be connected with an accretion disk located to the outer corona. Because of magnetorotational instabilities, the magnetic field will excite the fluctuation in the accretion rate in the accretion disk (Hawley & Balbus 1991; Balbus & Hawley 1998; Balbus 2005; Beckwith et al. 2008; Dexter & Fragile 2011). The fluctuation in the mass accretion rate will cause variable emission. Then this mechanism will cause a variable-input soft-photon flux. The variable seed photon is upscattered in the corona to higher energy radiation. Besides, by comparing the rms ratios between L_2, L_3, and L_4, we can find that with increasing energy, more and more variable high-energy photons come from L_3 rather than L_2. In other words, the radiation region that L_3 corresponds to should be hotter than that of L_2. As for L_4 and L_3, the decreasing trend can be interpreted by different variable seed photon fluxes in the Comptonization process. If we consider a radially extended corona, L_3 comes from the outer region whereas L_4 comes from the inner region; the inner region contributes more radiation than the outer region at 1–150 keV. In other words, the rms ratio between L_4 and L_3 should always be higher than 1. Meanwhile, we should note that the inner region receives more variable soft photons than the outer region. The inner region not only receives soft photons from the disk but also from the outer region. The flux from the outer region should be more variable than the flux from the standard accretion disk. This phenomenon has been reported in Dziełak et al. (2021); most of the disk photons upscattered in the outer Comptonization region (Zone II) are used as seed photons for the inner Comptonization region. Therefore, the decreasing slope of the fractional rms with the energy for L_4 should be greater than that for L_3, which means a downward trend for the L_4/L_3 rms ratio with the energy.

Then, the energy dependence of the characteristic frequency is comparatively complicated. For the L_2 and L_3 components, the characteristic frequency keeps almost constant below 20–30 keV; then it increases with the energy up to 90–150 keV. For the L_4 component, the characteristic frequency always increases with the energy from 1 to 150 keV. When the energy is below 20–30 keV, the constant characteristic frequency for L_2 and L_3 may reflect the relatively uniform radiation area in the outer region. However, when the energy is above 30 keV, the increasing characteristic frequency of L_2 and L_3 may reflect the increasing optical depth in the hot flow from the outer to the inner region. (This will be discussed in Section 4.4.)

In summary, the energy dependence of the fractional rms and characteristic frequency indicates that a complicated stratified accretion flow consisting of multiple coronae is need.

4.4. Phase-lag Spectra

As shown in Figure 11, at frequencies above QPO, the value of the phase lag is positive and frequency-dependent. The positive lag means that hard emission lags the soft one. According to the fluctuation propagating model, hard photons coming from the inner region will lag behind soft photons coming from the outer region (Kotov et al. 2001). More interestingly, there are two humps in Figure 11. From Figure 11, we can approximately see that $\nu_{g1} \simeq \nu_{L3}$ and $\nu_{g2} \simeq \nu_{L2}$. This correspondence is very similar to the simulation results of Rapisarda et al. (2017a). According to the PROPFLUC model developed by Ingram & Done (2012), if we consider a disk+corona geometry, then we will also have two humps in the phase-lag spectra as two visible humps in the PDS (Rapisarda et al. 2014, 2016a, 2016b, 2017a, 2017b).

In addition, as Figure 12 shows, the energy dependence of the phase lag also reflects that harder photons come from the inner region and cause a greater delay (Kotov et al. 2001).

In summary, by combining the power spectra and phase-lag spectra, we speculate that L_2 originates from the outer region whereas L_3 and L_4 originate from the inner region. Meanwhile, we confirm the applicability of the fluctuation propagation model.

4.5. Implication for Accretion Structure

In this paper, we investigate the accretion flow qualitatively at the LE, ME, HE bands and the quantitative fitting will be done in the next paper.

Dziełak et al. (2021) found significant spectral differences among Lorentzians for MAXI J1820+070 using the NICER 0.3–10 keV data. The model they presented comprises an outer Comptonization region fueled by thermal photons from the cool disk, and an inner Comptonization region fueled by a fraction of the upscattered photons from the outer Comptonization region. Similarly, Kawamura et al. (2022) also model the spectra and timing variability of MAXI J1820+070 to assume a geometry consisting of a variable disk and two hot-flow regions. As for this paper, we also have found the two-hump structure in the PDS reported in the abovementioned papers and one more QPO component in the LE, ME, and HE bands. According to Kawamura et al. (2022), the dip in the PDS is assumed to be caused by a drop in the viscous timescale between the accretion disk and hot flow (Rapisarda et al. 2017b; Kawamura et al. 2022). The different viscous timescale between the disk and hot flow are physically natural because the scale height H/R of the accretion flow is expected to be different between these regions (Narayan et al. 1997). Thus, we see two evident humps in the PDS (separately L_2 and L_3, L_4).

In addition to the common evolutionary trend for L_2, L_3, and L_4, L_3 shows a more sophisticated evolution trend. L_3 first appears in all three energy bands in ObsID P0114661002, but as the hardness decreases, L_3 disappears in the LE band first and then disappears in the ME band after nine ObsIDs ($\sim$18 days). This may implicate a change in the emitting spectrum where L_3 originates: when the hardness ratio is less than 0.61,

the region represented by L_3 emits a relatively hard spectrum so that L_3 only appears in the HE PDS. The distinct evolution trend of L_3 highlights the strong contrast with L_2 and L_4.

Then we investigate the hot accretion flow to explain other results, especially the energy dependence of L_3 and L_4. Similar to the argument presented by Kawamura et al. (2022), we attribute L_3 to the outer corona while L_4 comes from the inner corona. The fluctuation propagation model predicts that the characteristic frequency of broadband noise is inversely proportional to the radius. In view of the toy model we discussed, considering the relation between the characteristic frequency and photon energy, we speculate that the region farther from the black hole in the outer corona has a relatively uniform distribution in parameters such as the density and temperature to cause the constant frequency below 20–30 keV for L_3. Then when the photon energy is greater than 20–30 keV, with increasing optical depth, the emitted spectrum becomes harder at a smaller radius to cause increasing characteristic frequency. This explanation also applies to L_4, only with more seed photons from the outer corona. Then we use the energy dependence of the characteristic frequency to make a simple quantitative estimation. We consider that the outer radius of the hot flow r_{out} equals the inner radius of the accretion disk $r_{disk} \sim 27R_g$ (see Figure 13). It is difficult to connect the characteristic frequency with regions of the hot flow because of the current poor understanding of hot flows. Nevertheless, because the break frequency of the broadband noise component is proportional to $r^{-3/2}$ in the hot flow, the inner radius of the outer corona is $r_{in1} \sim 20R_g$ and the inner radius of the inner corona is $r_{in2} \sim 7R_g$. In calculation, we assume that the 90–150 keV radiation comes from the inner-most region of each corona, and 1–3 keV radiation comes from the outer region. This result is basically consistent with that in Kawamura et al. (2022) and $R_{in} \gtrsim 10R_g$ as in De Marco et al. (2021).

All discussions above are based on the two-coronae model. In fact, we note that there are still some results that are not easy to interpret. For instance, in Figures 7, 8, we observe the disappearance of L_3 in the LE and ME energy bands as the spectrum evolves. In the two-coronae model, the emission region that L_3 represents is located between the outer accretion disk and inner corona. It is relatively difficult to explain why L_3 emits such hard spectra when the hardness ratio is less than ~ 0.61. Besides, from Figure 9, when the photon energy is less than 20–30 keV, the characteristic frequency of L_2 and L_3 shows no evident change. It seems to be contrary to our usual understanding that harder photons come from the inner region. As a result, as Rapisarda et al. (2017b), Mushtukov et al. (2018), and other paper discuss (Marino et al. 2021), we may consider a more sophisticated accretion flow geometry (such as bending wave, viscous diffusion, outward fluctuation propagation effect, hot jet-emitting disk) and multiwavelength observations to explain all the results. To sum up, MAXI J1820+070 is an ideal laboratory to study inhomogeneous stratified coronae.

Except the model we discuss in this paper, similar to the model assuming that the QPO comes from jet precession (Ma et al. 2021), we can also attribute broadband noise to jet contribution (Markoff et al. 2005; Nowak et al. 2011). It should be note that the results in Ma et al. (2021) reveal the relationship between the jet precession and the LFQPO in the high-energy band; the jet precession model does not depend on

whether the accretion disk is truncated. Malzac (2013) has proposed the internal shock model to consider the effect of fluctuation in an accretion flow on jet ejecta. In particular, in Wang et al. (2020), by studying the hard time lag in the high-frequency range, the high-frequency time lags are significantly correlated to the photon index derived from the fit to the quasi-simultaneous NICER spectrum. They suggested that this result is qualitatively consistent with a model in which the high-frequency time lags are produced by Comptonization in a jet. As Wang et al. (2020) showed, the evolution of the high-frequency lags is highly correlated to that of the photon index of the hard spectral component by integrating the continuum broadband noise. Different from the method used in Wang et al. (2020), we investigate the broadband noise components through the Lorentzian function fitting method and mainly focus on the energy dependence of each component in the PDS. Overall, the results in Wang et al. (2020), Ma et al. (2021), and our work suggest that there are two hard emission regions during the studied period of the outburst in MAXI J1820: one is a hot-flow-like corona and the other is a jet. As a result, this model needs further investigation for connecting the hot flow and jet base.

5. Conclusion

In summary, a radial-stratified hot flow with a truncated accretion disk is needed to explain our results based on the fluctuation propagating model. We should combine timing analysis and spectral fitting, especially in the HE energy band, to improve our understanding of inhomogeneous coronae in the future.

ORCID iDs

He-Xin Liu ● https://orcid.org/0000-0002-1744-1641
Wei Yu ● https://orcid.org/0000-0002-3229-2453
L. Tao ● https://orcid.org/0000-0002-2705-4338
J. L. Qu ● https://orcid.org/0000-0002-9796-2585
S. N. Zhang ● https://orcid.org/0000-0001-5586-1017
L. M. Song ● https://orcid.org/0000-0003-0274-3396
S. M. Jia ● https://orcid.org/0000-0002-5203-8321
D. K. Zhou ● https://orcid.org/0000-0002-7420-9988

References

Altamirano, D., & Méndez, M. 2015, MNRAS, 449, 4027
Arnaud, K. A. 1996, in ASP Conf. Ser. 101, Astronomical Data Analysis Software and Systems V, ed. G. H. Jacoby & J. Barnes (San Francisco, CA: ASP), 17
Astropy Collaboration, Robitaille, T. P., Tollerud, E. J., et al. 2013, A&A, 558, A33
Atri, P., Miller-Jones, J. C. A., Bahramian, A., et al. 2020, MNRAS, 493, L81
Axelsson, M., Hjalmarsdotter, L., & Done, C. 2013, MNRAS, 431, 1987
Bailer-Jones, C. A. L., Rybizki, J., Fouesneau, M., Demleitner, M., & Andrae, R. 2021, AJ, 161, 147
Balbus, S. A. 2005, in ASP Conf. Ser. 330, The Astrophysics of Cataclysmic Variables and Related Objects, ed. J. M. Hameury & J. P. Lasota (San Francisco, CA: ASP), 185
Balbus, S. A., & Hawley, J. F. 1998, RvMP, 70, 1
Beckwith, K., Hawley, J. F., & Krolik, J. H. 2008, MNRAS, 390, 21
Belloni, T., & Hasinger, G. 1990, A&A, 227, L33
Belloni, T., Homan, J., Casella, P., et al. 2005, A&A, 440, 207
Belloni, T., Psaltis, D., & van der Klis, M. 2002, ApJ, 572, 392
Belloni, T., van der Klis, M., Lewin, W. H. G., et al. 1997, A&A, 322, 857
Belloni, T. M. 2010, in The Jet Paradigm, Lecture Notes in Physics, Vol. 794, ed. T. M. Belloni (Berlin : Springer), 53
Belloni, T. M., & Motta, S. E. 2016, in Astrophysics of Black Holes: From Fundamental Aspects to Latest Developments, ed. C. Bambi (Berlin: Springer), 61
Belloni, T. M., Motta, S. E., & Muñoz-Darias, T. 2011, BASI, 39, 409
Belloni, T. M., & Stella, L. 2014, SSRv, 183, 43
Bright, J. S., Fender, R. P., Motta, S. E., et al. 2020, NatAs, 4, 697
Bu, Q., Belloni, T. M., Chen, L., & Qu, J. 2017, ApJ, 841, 122
Buisson, D. J. K., Fabian, A. C., Barret, D., et al. 2019, MNRAS, 490, 1350
Bult, P., & van der Klis, M. 2015, ApJ, 806, 90
Cao, X., Jiang, W., Meng, B., et al. 2020, SCPMA, 63, 249504
Chen, Y., Cui, W., Li, W., et al. 2020, SCPMA, 63, 249505
Chen, Y. P., Zhang, S., Qu, J. L., et al. 2018, ApJL, 864, L30
De Marco, B., Zdziarski, A. A., Ponti, G., et al. 2021, A&A, 654, A14
Denisenko, D. 2018, ATel, 11400, 1
Dexter, J., & Fragile, P. C. 2011, ApJ, 730, 36
Done, C., Gierliński, M., & Kubota, A. 2007, A&ARv, 15, 1
Dziełak, M. A., De Marco, B., & Zdziarski, A. A. 2021, MNRAS, 506, 2020
Esin, A. A., McClintock, J. E., & Narayan, R. 1997, ApJ, 489, 865
Fiori, M., Zampieri, L., Burtovoi, A., et al. 2018, ATel, 11824, 1
Gierliński, M., & Zdziarski, A. A. 2005, MNRAS, 363, 1349
Gleissner, T., Wilms, J., Pottschmidt, K., et al. 2004, A&A, 414, 1091
Guan, J., Tao, L., Qu, J. L., et al. 2021, MNRAS, 504, 2168
Hawley, J. F., & Balbus, S. A. 1991, ApJ, 376, 223
Homan, J., Bright, J., Motta, S. E., et al. 2020, ApJL, 891, L29
Huang, Y., Qu, J. L., Zhang, S. N., et al. 2018, ApJ, 866, 122
Huang, Y., Zhang, S.-N., & Qu, J. 2021, in 43rd COSPAR Scientific Assembly, 1585
Hunter, J. D. 2007, CSE, 9, 90
Huppenkothen, D., Bachetti, M., Stevens, A., et al. 2019a, JOSS, 4, 1393
Huppenkothen, D., Bachetti, M., Stevens, A. L., et al. 2019b, ApJ, 881, 39
Ingram, A., & Done, C. 2012, MNRAS, 419, 2369
Ingram, A., Done, C., & Fragile, P. C. 2009, MNRAS, 397, L101
Ingram, A. R. 2016, AN, 337, 385
Ingram, A. R., & Motta, S. E. 2019, NewAR, 85, 101524
Kara, E., Steiner, J. F., Fabian, A. C., et al. 2019, Natur, 565, 198
Kato, S., Fukue, J., & Mineshige, S. 2008, Black-Hole Accretion Disks—Towards a New Paradigm (Kyoto: Kyoto Univ. Press)
Kawamura, T., Axelsson, M., Done, C., & Takahashi, T. 2022, MNRAS, 511, 536
Kawamuro, T., Negoro, H., Yoneyama, T., et al. 2018, ATel, 11399, 1
Kotov, O., Churazov, E., & Gilfanov, M. 2001, MNRAS, 327, 799
Li, Z., Lei, Y., Qu, J., Zhang, S., & Song, L. 2010, SCPMA, 53, 86

Li, Z. B., Song, L. M., Qu, J. L., et al. 2012, Ap&SS, 341, 383
Liu, C., Zhang, Y., Li, X., et al. 2020, SCPMA, 63, 249503
Liu, H.-X., Huang, Y., Xiao, G.-C., et al. 2021, RAA, 21, 070
Lyubarskii, Y. E. 1997, MNRAS, 292, 679
Ma, X., Tao, L., Zhang, S.-N., et al. 2021, NatAs, 5, 94
Mahmoud, R. D., & Done, C. 2018a, MNRAS, 473, 2084
Mahmoud, R. D., & Done, C. 2018b, MNRAS, 480, 4040
Malzac, J. 2013, MNRAS, 429, L20
Marino, A., Barnier, S., Petrucci, P. O., et al. 2021, A&A, 656, A63
Markoff, S., Nowak, M. A., & Wilms, J. 2005, ApJ, 635, 1203
Matsuoka, M., Kawasaki, K., Ueno, S., et al. 2009, PASJ, 61, 999
Mikolajewska, J., Zdziarski, A. A., Ziolkowski, J., Torres, M. A. P., & Casares, J. 2022, ApJ, 930, 9
Mineshige, S., Takeuchi, M., & Nishimori, H. 1994, ApJL, 435, L125
Miyamoto, S., Kimura, K., Kitamoto, S., Dotani, T., & Ebisawa, K. 1991, ApJ, 383, 784
Mushtukov, A. A., Ingram, A., & van der Klis, M. 2018, MNRAS, 474, 2259
Mushtukov, A. A., Lipunova, G. V., Ingram, A., et al. 2019, MNRAS, 486, 4061
Narayan, R., Kato, S., & Honma, F. 1997, ApJ, 476, 49
Negoro, H., & Mineshige, S. 2002, PASJ, 54, L69
Nolan, P. L., Gruber, D. E., Matteson, J. L., et al. 1981, ApJ, 246, 494
Nowak, M. A., Hanke, M., Trowbridge, S. N., et al. 2011, ApJ, 728, 13
Nowak, M. A., Vaughan, B. A., Wilms, J., Dove, J. B., & Begelman, M. C. 1999, ApJ, 510, 874
Psaltis, D., Belloni, T., & van der Klis, M. 1999, ApJ, 520, 262
Rao, F., Belloni, T., Stella, L., Zhang, S. N., & Li, T. 2010, ApJ, 714, 1065
Rapisarda, S., Ingram, A., Kalamkar, M., & van der Klis, M. 2016a, MNRAS, 462, 4078
Rapisarda, S., Ingram, A., & van der Klis, M. 2014, MNRAS, 440, 2882
Rapisarda, S., Ingram, A., & van der Klis, M. 2016b, AN, 337, 524
Rapisarda, S., Ingram, A., & van der Klis, M. 2017a, MNRAS, 472, 3821
Rapisarda, S., Ingram, A., & van der Klis, M. 2017b, MNRAS, 469, 2011
Ratti, E. M., Belloni, T. M., & Motta, S. E. 2012, MNRAS, 423, 694
Remillard, R. A., & McClintock, J. E. 2006, ARA&A, 44, 49
Schnittman, J. D., Homan, J., & Miller, J. M. 2006, ApJ, 642, 420
Shakura, N. I., & Sunyaev, R. A. 1973, A&A, 500, 33
Sobolewska, M. A., & Życki, P. T. 2006, MNRAS, 370, 405
Stern, B. E., & Svensson, R. 1996, ApJL, 469, L109
Stiele, H., & Kong, A. K. H. 2020, ApJ, 889, 142
Stiele, H., & Yu, W. 2014, MNRAS, 441, 1177
Stiele, H., & Yu, W. 2015, MNRAS, 452, 3666
Terrell, N., & James, J. 1972, ApJL, 174, L35
Thomas, J. K., Buckley, D. A. H., Charles, P. A., et al. 2022, MNRAS, 513, L35
Torres, M. A. P., Casares, J., Jiménez-Ibarra, F., et al. 2019, ApJL, 882, L21
Torres, M. A. P., Casares, J., Jiménez-Ibarra, F., et al. 2020, ApJL, 893, L37
Turner, S. G. D., & Reynolds, C. S. 2021, MNRAS, 504, 469
Uttley, P. 2004, MNRAS, 347, L61
Uttley, P., & McHardy, I. M. 2001, MNRAS, 323, L26
Uttley, P., McHardy, I. M., & Vaughan, S. 2005, MNRAS, 359, 345
van der Walt, S., Colbert, S. C., & Varoquaux, G. 2011, CSE, 13, 22
Wang, Y., Ji, L., Zhang, S. N., et al. 2020, ApJ, 896, 33
Wijnands, R., & van der Klis, M. 1999, ApJ, 514, 939
Yu, W., Lin, J., Mao, D., et al. 2018, ATel, 11591, 1
Yu, W., & Zhang, W. 2013, ApJ, 770, 135
Zampieri, L., Fiori, M., Burtovoi, A., et al. 2018, ATel, 11723, 1
Zdziarski, A. A., Dziełak, M. A., De Marco, B., Szanecki, M., & Niedźwiecki, A. 2021a, ApJL, 909, L9
Zdziarski, A. A., Jourdain, E., Lubiński, P., et al. 2021b, ApJL, 914, L5
Zhang, L., Wang, Y., Méndez, M., et al. 2017, ApJ, 845, 143
Zhang, S.-N., Li, T., Lu, F., et al. 2020, SCPMA, 63, 249502
Zhang, W., & Yu, W. 2015, ApJ, 805, 139
Zhao, X., Gou, L., Dong, Y., et al. 2021, ApJ, 916, 108